Modeling heterogeneity and permeability evolution in a compaction band using a phase-field approach

Sabrina C.Y. Ip[1] · Ronaldo I. Borja[1,*]

[1]Department of Civil and Environmental Engineering, Stanford University, Stanford, CA 94305, USA. *E-mail: borja@stanford.edu

Summary. Compaction bands are tabular zones of localized compressive deformation associated with porosity and permeability reduction. Depending on their orientation, compaction bands can act as barriers to fluid flow, and can be detrimental to fluid production in oil and gas reservoirs, as well as in CO_2 sequestration. The process of permeability reduction and the development of excess pore pressures during compaction band formation in a heterogeneous rock mass are not fully understood. Furthermore, few studies have modeled compaction band formation considering coupled hydromechanical processes. In this study, we propose a coupled hydromechanical, phase-field approach for capturing the formation and propagation of compaction bands in heterogeneous porous media. Breakage mechanics is adopted to characterize the free energy function in the intact and damaged material. The resulting phase-field variable provides a measure of the degree of grain crushing. Permeability reduction in the zone of compaction localization is modeled using the Kozeny-Carman equation accounting for microstructural evolution. Numerical simulations demonstrate the ability of the model to capture compaction band formation, porosity reduction, and permeability evolution under drained and undrained conditions. The results highlight the role of effective confining pressure, drainage conditions, and material parameters on the styles of compaction bands that form.

Keywords. Compaction band, grain crushing, permeability evolution, phase-field, porous media

1 Introduction

Porous sedimentary rocks have worldwide economic importance as they are key hosts for groundwater and hydrocarbon reservoirs [93], CO_2 sequestration [101], and hazardous waste disposal [59]. The fluid injection, storage and extraction processes involved in these applications rely significantly on the mechanical and hydraulic properties of the host rocks. As such, structures and features that act as barriers for fluid flow can have adverse impacts on

the properties of these rocks. One such feature is a compaction band, which is one type of deformation band that occurs as a thin, tabular zone of localized compaction [5, 18, 19, 56]. Compaction bands have been observed in various high-porosity rocks, including sandstones [40, 46, 48, 72, 91, 92, 114, 122], limestone [102], and volcanic rock [44]. Depending on their orientation, and microtexture, compaction bands can be categorized into either pure or shear-enhanced compaction bands [40]. The shear-enhanced compaction bands include straight tabular compaction bands that form obliquely (38–53°) to the direction of maximum principal stress [40, 56], and wiggly bands with wavelengths of several centimeters [79]. Wiggly bands consist of individual segments of oblique compaction bands that generally develop perpendicular to the direction of maximum principal stress. In contrast, pure compaction bands are straight bands that develop perpendicular to the direction of maximum principal stress.

Compaction bands can result in significant porosity and permeability reduction, unlike shear bands that can also exhibit dilative behavior [5]. Oftentimes, compaction bands exhibit signs of grain damage, cataclastic pore collapse, and preferential clay accumulation [40, 70]. Previous studies suggest that compaction band initiation and propagation can be triggered by spatially heterogeneous material properties [30, 35, 46, 57]. Compaction bands have been found to initiate at high porosity zones in Bleurswiller sandstone [46] and Mount Gambier limestone [30]. There is also evidence of continued diffusive growth within these zones of higher porosity [30, 46]. As such, compaction band formation generally results in microstructural evolution of the rock's material properties, which in turn can change its mechanical and hydraulic behavior. There has also been evidence of borehole breakout resulting from compaction localization [39, 53, 54]. Thus, it is desirable to develop models that capture the formation and propagation of compaction bands with the added ability to realistically predict the evolution of heterogeneity and permeability of the rock.

There have been a number of studies on the development of compaction bands in high porosity rocks [1, 7, 9, 11, 28, 93, 103, 109, 111]. A handful of these studies have focused on the effects of compaction localization on permeability reduction [8, 47, 59, 115, 139]. Laboratory-scale experiments have identified the macroscopic hydromechanical response and microstructural alterations in and around the vicinity of the compaction band [38]. The permeability has been found to vary with several orders of magnitude difference between inside and outside the localization zone within the same rock sample [8, 115]. Factors controlling the permeability reduction in the compaction band include the reduction in porosity, the specific surface area, and the average aspect ratio of the band [47, 115]. In addition, the evolution in the pore shape and grain orientations during compaction band formation can also lead to anisotropic permeability in porous rocks [8]. However, most studies conducted tests under drained conditions, and there is limited understanding of the failure patterns under undrained conditions [109].

Mechanistic models have been proposed to capture the formation of compaction bands in porous rocks. The 'anticrack' model proposed by Mollema and Antonellini [87] and Sternlof et al. [108] uses an analog to linear elastic fracture mechanics to describe the stress distribution around the tip of a compaction band, in which the 'free faces' of the crack are allowed to overlap (a reverse kinematics to the mode-I crack opening). The bifurcation approach proposed by Rudnicki and Rice [99] has also been used to predict compaction band formation [27, 65]. Some authors adopted micromechanics-based approaches, such as spring network models and discrete element models [68, 69, 79, 81, 117, 123, 125], which have offered insight into the formation and propagation of compaction bands at the grain scale. Other studies incorporated the breakage mechanics framework [41, 42] coupled with plasticity to capture grain crushing and track the progression of the compaction band [36, 90, 113]. Recently, the phase-field approach has been adopted in several studies to model compaction band formation [62, 116]. The phase-field approach is based on the variational approach to fracture [49], in which the crack is approximated as a diffuse interface represented by the phase-field variable, and has been extended to model fractures in rocks [34, 45, 126, 138]. Ip and Borja [62] developed a phase-field formulation for modeling compaction bands in rocks employing breakage mechanics and critical state plasticity. They showed that the development of different types of compaction band patterns was influenced by material properties such as the plasticity model parameters, the critical fracture energy G_c and the grading index θ, as well as loading conditions such as the confining pressure. Additionally, they highlighted the importance of spatially varying material parameters on the development of different compaction band patterns. Wang et al. [116] also adopted a phase-field approach to model compaction band formation under dynamic loading conditions.

Simultaneously, there has been an extensive body of work on modeling the permeability evolution under applied stresses, accounting for porosity reduction and an increase in the specific surface. A variety of methods have been used to model the hydraulic behavior, including empirical formulations [37], capillary models [71], statistical approaches [66], and hydraulic radius theories [140]. Among the empirical models, most are generalizations of the Kozeny-Carman model [26, 73]. The evolution of the microstructure during deformation needs to be tracked to accurately capture the permeability reduction when a compaction band forms. Since breakage mechanics can capture changes in the microstructure, including the porosity and specific surface area, models based on breakage mechanics have been used to study the permeability evolution in rocks using a Kozeny law [43, 89].

Few studies have proposed hydromechanical formulations that account for permeability reduction resulting from grain crushing and microstructure evolution [52, 75, 88, 124]. Wu et al. [124] presented a multiscale modeling approach using FEM/DEM to model compaction bands in specimens under dry, drained, and undrained conditions. However, they only considered pore

collapse and inter-granular debonding as the primary micromechanisms and neglected the effects of grain crushing. Continuum approaches have also been developed adopting breakage mechanics and nonlocal regularization to track grain crushing in porous rocks [52, 88]. Common enrichment techniques employed for this purpose include the embedded strong discontinuity and extended finite element methods [16, 17, 20, 77, 78].

In this present study, we extend our previous phase-field formulation to model compaction band formation in porous media. The phase-field formulation adopts a free-energy decomposition inspired by breakage mechanics that is suitable for modeling compaction band formation, as well as utilizes the modified Cam-Clay plasticity model to describe the inelastic material behavior [21]. We couple the phase-field formulation with the governing equations for fluid flow in a fully-saturated isotropic porous media. Flow in the porous media is assumed to follow Darcy's law and the Kozeny-Carman equation is used to describe the evolution of permeability due to changes in the porosity and grain size distribution. Subsequently, we demonstrate the ability of the model to capture various compaction band shapes, including pure compaction and shear-enhanced compaction bands, under drained and undrained conditions, as well as the evolution of permeability in the sample. Finally, we investigate the effects of heterogeneous porosity on compaction band formation in a natural rock [30] under different drainage conditions. We note that the proposed mechanistic model only considers grain crushing in fully dry and fully saturated conditions as the cause of compaction band formation, and ignores the effects of degree of saturation [61, 63, 64] and creep [23, 76, 130].

2 Theory

In this section, we combine the phase-field formulation for compaction band formation proposed by Ip and Borja [62] with balance of mass for the solid-fluid mixture, thereby introducing the pore fluid pressure p as an additional variable. As in the previous work, we assume the deformation to be infinitesimal and take the phase-field variable d as a measure of grain crushing.

2.1 Governing equations

Let $\mathcal{B}$ define the domain of the body with external boundary $\partial\mathcal{B}$. We assume that the boundary can be decomposed into essential and natural boundaries $\partial\mathcal{B}_u$ and $\partial\mathcal{B}_t$, where displacement and surface tractions are prescribed, respectively; and $\partial\mathcal{B}_p$ and $\partial\mathcal{B}_q$, where fluid pressure and flux are prescribed, respectively. The linear momentum balance takes the form

$$\left.\begin{aligned} \nabla\cdot\boldsymbol{\sigma}+\rho\boldsymbol{g}=\boldsymbol{0} \quad &\text{in} \quad \mathcal{B} \\ \boldsymbol{n}\cdot\boldsymbol{\sigma}=\bar{\boldsymbol{t}} \quad &\text{on} \quad \partial\mathcal{B}_t \\ \boldsymbol{u}=\bar{\boldsymbol{u}} \quad &\text{on} \quad \partial\mathcal{B}_u \end{aligned}\right\}, \tag{1}$$

where $\boldsymbol{\sigma}$ is the total Cauchy stress tensor, ρ is the mass density, $\boldsymbol{g}$ is the gravitational acceleration vector, $\boldsymbol{n}$ is the outward unit normal vector to the boundary $\partial\mathcal{B}_t$ on which the surface traction $\bar{\boldsymbol{t}}$ is prescribed, and $\bar{\boldsymbol{u}}$ is the prescribed value of displacement field $\boldsymbol{u}$ on the boundary $\partial\mathcal{B}_u$.

We assume that the pore space is fully occupied by one type of fluid. For an isotropic porous medium, the balance of mass can be expressed as

$$\left.\begin{aligned} b\mathbf{1} : \dot{\boldsymbol{\epsilon}} + \frac{\phi}{K_w}\dot{p} + \boldsymbol{\nabla}\cdot\boldsymbol{q} = 0 \quad &\text{in} \quad \mathcal{B} \\ -\hat{\boldsymbol{n}}\cdot\boldsymbol{q} = \bar{q} \quad &\text{on} \quad \partial\mathcal{B}_q \\ p = \bar{p} \quad &\text{on} \quad \partial\mathcal{B}_p \end{aligned}\right\}, \tag{2}$$

where

$$b = 1 - \frac{K}{K_s} \tag{3}$$

is the Biot coefficient, $\boldsymbol{\epsilon}$ is the total strain tensor, $\mathbf{1}$ is the identity tensor, K is the drained bulk modulus of the solid skeleton, K_w is the bulk modulus of water, K_s is the bulk modulus of the solid constituent, ϕ is the porosity, $\boldsymbol{q}$ is the Darcy flux, $\hat{\boldsymbol{n}}$ is the outward unit normal vector to the boundary $\partial\mathcal{B}_q$ on which the normal fluid flux $\bar{q}$ is prescribed, and $\bar{p}$ is the prescribed value of the pore pressure p on the boundary $\partial\mathcal{B}_p$. The superimposed dot is the material time derivative following the solid motion.

The total Cauchy stress tensor $\boldsymbol{\sigma}$ may be decomposed into an effective stress tensor $\boldsymbol{\sigma}'$ and pore fluid pressure p according to the effective stress equation

$$\boldsymbol{\sigma} = \boldsymbol{\sigma}' - bp\mathbf{1}\,. \tag{4}$$

We refer the readers to more recent articles [134–136] for developments appropriate for anisotropic porous media.

The porous material may also contain an internal discontinuity, such as a compaction band, denoted by Γ. The presence of a discontinuous strain field in the zone of discontinuities is difficult to track using conventional numerical modeling techniques. As such, we follow the standard phase-field modeling approach suggested in Miehe et al. [83], in which the discontinuous strain field is regularized by introducing a phase-field variable $d \in [0,1]$ that represents the degree of micro-structural changes in the material. In the framework proposed by Ip and Borja [62], d represents the degree of grain crushing. A completely intact region is denoted by the value of the phase-field variable $d = 0$, whereas a completely crushed zone is defined by the value $d = 1$. The strain jump in the damaged zone can then be approximated by introducing a compaction-zone density functional $\gamma(d, \nabla d)$ [25]

$$\begin{aligned} \int_\Gamma \mathcal{G}_c \,\mathrm{d}A &\approx \int_\mathcal{B} \mathcal{G}_c \gamma(d, \nabla d)\,\mathrm{d}V \\ &= \int_\mathcal{B} \mathcal{G}_c \Big(\frac{d^2}{2l_0} + \frac{l_0}{2}\nabla d\cdot\nabla d\Big)\,\mathrm{d}V\,, \end{aligned} \tag{5}$$

where $\mathcal{G}_c$ is the critical energy release rate [100, 111, 114] and l_0 is the length parameter controlling the width of the phase-field approximation zone. The phase-field evolution can then be expressed as

$$\left.\begin{aligned} \mathcal{G}_c l_0 \nabla^2 d - \mathcal{G}_c \frac{d}{l_0} - \frac{\partial \psi}{\partial d} = 0 \quad \text{in} \ \ \mathcal{B} \\ \nabla d \cdot \boldsymbol{n} = 0 \quad \text{on} \ \ \partial\mathcal{B} \end{aligned}\right\}, \tag{6}$$

where ψ is the stored energy density and ∇^2 is the Laplacian operator. The following section reviews the form of ψ developed in Ip and Borja [62] that is appropriate for modeling compaction band formation and propagation.

2.2 Free energy decomposition for breakage

Ip and Borja [62] proposed a novel free energy decomposition in which breakage mechanics theory is used to degrade the elastic modulus from its initial value at the intact state to its final value at the completely crushed state. Continuum breakage mechanics is a thermodynamically consistent constitutive model developed by Einav [41, 42] to predict the evolution of the grain size distribution in granular materials. In breakage mechanics, a macroscopic internal variable B, is introduced to track the degree of grain crushing in the material. The stored energy density proposed in Ip and Borja [62] uses the phase-field variable as a measure of the degree of grain crushing.

For the elastic free energy density, we take advantage of the spectral strain decomposition proposed by Miehe [83] for an isotropic material to split the elastic strain $\boldsymbol{\epsilon}^e$, into a tension part, $\boldsymbol{\epsilon}^{e+}$, and a compression part $\boldsymbol{\epsilon}^{e-}$, with

$$\boldsymbol{\epsilon}^{e\pm} = \sum_{a=1}^{3} \langle \epsilon_a \rangle_{\pm} \boldsymbol{n}^{(a)} \otimes \boldsymbol{n}^{(a)} , \tag{7}$$

where ϵ_a and $\boldsymbol{n}^{(a)}$ are the principal strains and principal directions, respectively, and $\boldsymbol{n}^{(a)} \otimes \boldsymbol{n}^{(a)}$ is the corresponding spectral direction. The elastic stored energy density function can also be split into a tension-related energy function and a compressive energy function

$$\psi^e(\boldsymbol{\epsilon}^e, d) = \psi^{e+}(\boldsymbol{\epsilon}^p, d) + \psi^{e-}(\boldsymbol{\epsilon}^p, d) . \tag{8}$$

Based on breakage mechanics, Ip and Borja [62] developed the following expression for the compressive elastic free energy

$$\psi^{e-}(\boldsymbol{\epsilon}^e, d) = g(d)\theta\psi_0^{e-}(\boldsymbol{\epsilon}^e) + (1-\theta)\psi_0^{e-}(\boldsymbol{\epsilon}^e) . \tag{9}$$

where $g(d)$ is a degradation function commonly defined as $g(d) = (1-k)(1-d)^2 + k$, and $0 < k \ll 1$ is a stability parameter introduced to avoid numerical singularities when the phase-field variable approaches the value 1 [12, 13, 83,

85]. The grading index, $\theta = 1 - \psi_u^e/\psi_0^e$, is a scalar variable that describes the relationship between the undamaged elastic free energy ψ_0^e and the remaining free energy ψ_u^e. This allows us to represent the elastic compressive free energy only in terms of the elastic free energy in the undamaged state.

It then follows that

$$\psi^e(\boldsymbol{\epsilon}^e, d) = g(d)\Big(\psi^{e+}(\boldsymbol{\epsilon}^e) + \theta\psi_0^{e-}(\boldsymbol{\epsilon}^e)\Big) + (1-\theta)\psi_0^{e-}(\boldsymbol{\epsilon}^e)\,. \tag{10}$$

and the effective stress tensor can be written as

$$\boldsymbol{\sigma}' = g(d)(\boldsymbol{\sigma}'^{+}_0 + \theta\boldsymbol{\sigma}'^{-}_0) + (1-\theta)\boldsymbol{\sigma}'^{-}_0\,. \tag{11}$$

Several studies have highlighted the importance of tensile microcracks in the formation of shear-enhanced compaction bands [3,4], which suggests that the tensile free energy contributes to the formation of compaction bands. We note the importance of accommodating for the development of tensile stresses in regions close to the imperfections, since tensile stresses could also impact the direction of propagation of the compaction band. Thus, we also apply the same degradation function $g(d)$ to the tension regime. However, since the material is undergoing compressive axial strain, there is little development of the tension-related elastic free energy and the tensile stresses do not develop to the extent that a tensile crack propagates through the sample. As such, the evolution of the phase-field variable is not an indication of fracture or cracking under compressive loading conditions.

The plastic stored energy density is also decomposed into tension and compression parts

$$\psi^p(\boldsymbol{\epsilon}^p, d) = \psi^{p+}(\boldsymbol{\epsilon}^p) + \psi^{p-}(\boldsymbol{\epsilon}^p, g(d))\,. \tag{12}$$

To account for the contribution of plastic straining towards compaction band formation, we assume only a portion of compactive plastic flow contributes to grain crushing [129, 131]

$$\psi^{p-} = \begin{cases} W^p & \text{if} \quad \mathrm{tr}(\boldsymbol{\epsilon}^p) \le 0 \\ 0 & \text{if} \quad \mathrm{tr}(\boldsymbol{\epsilon}^p) > 0 \end{cases} \tag{13}$$

$$\psi^{p+} = \begin{cases} 0 & \text{if} \quad \mathrm{tr}(\boldsymbol{\epsilon}^p) \le 0 \\ W^p & \text{if} \quad \mathrm{tr}(\boldsymbol{\epsilon}^p) > 0 \end{cases} \tag{14}$$

where W^p is the plastic free energy, which is related to the accumulated plastic work and can generally be defined as [4]

$$W^p = \int_0^t (1-\omega)\boldsymbol{\sigma} : \dot{\boldsymbol{\epsilon}}^p \mathrm{d}t\,, \tag{15}$$

where t is the current pseudo-time and $1-\omega$ is the Taylor-Quinney coefficient [110] that denotes the fraction of plastic work dissipated as heat and ranges

from 0 to 1. We assume the Taylor-Quinney coefficient to be 0.9 (i.e., $\omega = 0.1$) for all examples in this study.

Finally, the stored energy density for modeling compaction band formation can be expressed as

$$\psi(\boldsymbol{\epsilon}^e, \boldsymbol{\epsilon}^p, d) = g(d)\Big(\psi^{e+}(\boldsymbol{\epsilon}^e) + \theta\psi_0^{e-}(\boldsymbol{\epsilon}^e)\Big) + (1-\theta)\psi_0^{e-}(\boldsymbol{\epsilon}^e) + \psi^p(\boldsymbol{\epsilon}^p, d) \quad (16)$$

and the last term on the left-hand side of the phase-field evolution equation (6) can be rewritten as

$$\frac{\partial \psi}{\partial d} = g'(d)\mathcal{H}\,, \quad (17)$$

where

$$g'(d) = 2(1-k)(1-d) \quad (18)$$

and $\mathcal{H}$ is the phase-field driving force given by

$$\mathcal{H} = \psi^{e+} + \theta\psi_0^{e-} + \frac{\partial \psi^{p-}}{\partial g}\,. \quad (19)$$

2.3 Constitutive relations

Solid deformation

To close the boundary value problem, we assume the same solid deformation constitutive relations as the formulation presented in Ip and Borja [62]. Here, we briefly summarize the main features of the solid deformation model and simply refer the readers to Ip and Borja [62] for further details. From Eq. (7), the tension- and compression-related elastic free energies can be written as

$$\left.\begin{aligned} \psi^{e+} &= \lambda\frac{\langle \mathrm{tr}\boldsymbol{\epsilon}^e\rangle_+^2}{2} + \mu\boldsymbol{\epsilon}^{e+} : \boldsymbol{\epsilon}^{e+} \\ \psi_0^{e-} &= \lambda\frac{\langle \mathrm{tr}\boldsymbol{\epsilon}^e\rangle_-^2}{2} + \mu\boldsymbol{\epsilon}^{e-} : \boldsymbol{\epsilon}^{e-} \end{aligned}\right\}\,, \quad (20)$$

where λ and μ are the Lamé constants. Similarly, the stress-strain relationship can be written as

$$\boldsymbol{\sigma}'^{\pm}_0 = \lambda\langle \mathrm{tr}\boldsymbol{\epsilon}^e\rangle_\pm \mathbf{1} + 2\mu\boldsymbol{\epsilon}^{e\pm}\,. \quad (21)$$

We adopt the modified Cam-Clay (MCC) [14, 15, 60, 97] constitutive theory with a non-zero tensile strength to model plastic deformation. The yield function is given as

$$F(\boldsymbol{\sigma}', p_c) = \frac{q^2}{M^2} + (p_v - p_t)\big(p_v - p_c\big) \le 0\,, \quad (22)$$

where $p_v = \mathrm{tr}(\boldsymbol{\sigma}')/3$, $q = \sqrt{3/2}\|\boldsymbol{s}\|$, and $\boldsymbol{s} = \boldsymbol{\sigma}' - p_v\mathbf{1}$. The model parameters M, $p_t > 0$ and $p_c < 0$ represent the slope of the critical state line, the tensile strength, and the preconsolidation pressure, respectively.

Ip and Borja [62] enriched the hardening/softening law of the MCC model to capture the softening response when the grains crush and the subsequent hardening response when the crushed grains reach their stable positions. In this case, the preconsolidation pressure p_c varies with both the plastic volumetric strain $\varepsilon_v^p < 0$ and the phase-field variable d according to the equation

$$\frac{\dot{p}_c}{p_c} = -\frac{\dot{\varepsilon}_v^p}{\lambda^p} + g'(d)\frac{\dot{d}}{\lambda^d}\,, \tag{23}$$

where λ^p is a plastic compressibility parameter and λ^d is a phase-field compressibility parameter. The second term on the right-hand side allows the model to capture the momentary unstable response induced by grain crushing and the associated pore collapse, and is otherwise zero in the absence of grain crushing (i.e., $d = 0$).

Remark. In equation (34) of Ip and Borja [62], the volumetric component of the plastic strain rate (first term in the brackets on the far right-hand side) should be corrected to $(\partial f/\partial p)\mathbf{1}/3$.

Fluid flow

We assume Darcy's law to be valid, which takes the form

$$\boldsymbol{q} = -\frac{\kappa}{\mu_w}\cdot(\nabla p + \rho_w \boldsymbol{g})\,, \tag{24}$$

where $\boldsymbol{q}$ is the Darcy velocity, κ is the isotropic saturated permeability, μ_w is the dynamic viscosity of the fluid, and ρ_w is the mass density of water. We assume the material permeability remains isotropic even after the compaction band has formed.

The evolution of void ratio upon compressive loading has the form [60, 97]

$$e = e_0 + \frac{(1+e_0)(p_v - p_{v0})}{K} - (1+e_0)\lambda^p\left(\ln\left(\frac{p_c}{p_{c0}^*}\right) - \frac{g(d)-1}{\lambda^d}\right), \tag{25}$$

where e_0 is the initial void ratio, p_{v0} is the reference hydrostatic effective stress and p_{c0}^* is the preconsolidation pressure at which grain crushing begins.

The evolution of porosity can then be obtained with the following relationship

$$\phi = \frac{e}{1+e} \tag{26}$$

Several studies have linked permeability reduction in compaction bands not only to reduction of the porosity in the band but also to an increase in the specific surface area [89, 121, 139]. The surface area of the grains can be approximated from the grain-size distribution [32]. We assume the permeability to vary with the porosity and grain-size distribution by the Kozeny-Carman relationship [10, 26, 73]

$$\kappa = f D_p(d)^2 \frac{\phi^3}{(1-\phi)^2}\,, \tag{27}$$

where f is scaling factor and D_p is the average grain diameter. In continuum breakage mechanics, the grain size distribution evolves upon breakage, which implies that the average grain diameter is a function of the breakage parameter. In this formulation, the average grain diameter would be a function of the phase field variable, d. To determine the relationship between D_p and d, we define the average grain diameter as the harmonic mean of the grain size distribution, G,

$$\frac{1}{D_p} = \int_{D_{\min}}^{D_{\max}} \frac{G(D,d)}{D}\mathrm{d}D\,, \tag{28}$$

where D is a given grain diameter, $D_{\max}$ is the maximum grain size diameter and $D_{\min}$ is the minimum grain size diameter, which can be obtained experimentally.

The particle size distribution can be expressed in terms of the initial G_0 and ultimate G_u particle size distribution functions, when $d = 0$ and $d = 1$, respectively. The average grain diameter can then be written as [89]

$$\frac{1}{D_p} = (1-d)\frac{1}{D_{\max}} + d\frac{1}{D_{\min}}\,. \tag{29}$$

2.4 Finite element formulation

In this section, we describe the numerical implementation of the governing equations defined by Equations (1), (2), and (6). Let $\boldsymbol{\eta} \in \boldsymbol{\mathcal{U}}$, $\xi \in \mathcal{V}$, and $\zeta \in \mathcal{W}$ denote the weighting functions belonging in the appropriate sets $\boldsymbol{\mathcal{U}}$, $\mathcal{V}$, and $\mathcal{W}$, respectively. Applying the standard weighted residual procedure, integrating by parts, using the divergence theorem, and substituting the natural boundary conditions to Equations (1), (2), and (6) yields the variational equations for linear momentum balance, mass balance, and phase-field evolution of the forms

$$\left.\begin{aligned} \int_{\mathcal{B}} \nabla^s\boldsymbol{\eta} : \boldsymbol{\sigma}\,\mathrm{d}V &= \int_{\mathcal{B}} \boldsymbol{\eta}\cdot\rho\boldsymbol{g}\,\mathrm{d}V + \int_{\partial\mathcal{B}_t} \boldsymbol{\eta}\cdot\bar{\boldsymbol{t}}\,\mathrm{d}A \\ \int_{\mathcal{B}} \xi B\mathbf{1} : \nabla^s\boldsymbol{v}\,\mathrm{d}V + \int_{\mathcal{B}} \xi\frac{\phi}{K_w}\dot{p}\,\mathrm{d}V - \int_{\mathcal{B}} \nabla\xi\cdot\boldsymbol{q}\,\mathrm{d}V &= \int_{\partial\mathcal{B}_q} \xi\bar{q}\,\mathrm{d}A \\ \int_{\mathcal{B}} \mathcal{G}_c l_0 \nabla\zeta\cdot\nabla d\,\mathrm{d}V + \int_{\mathcal{B}} \zeta\mathcal{G}_c\frac{d}{l_0}\,\mathrm{d}V + \int_{\mathcal{B}} \zeta g'(d)\mathcal{H}\,\mathrm{d}V &= 0 \end{aligned}\right\}\,, \tag{30}$$

where $\nabla^s = (\nabla + \nabla^{\mathsf{T}})/2$ is the symmetric gradient operator.

This system of variational equations was implemented using the phase-field, porous flow, and tensor mechanics modules of the Multiphysics Object-Oriented Simulation Environment (MOOSE) framework [94, 119, 120] and discretized using mixed finite elements with equal-order interpolation on the

displacement, pore pressure and phase-field variables, but with a stabilization feature that ensures satisfaction of the weak inf-sup condition [118]. A staggered procedure was adopted for solving the coupled equations in which the poromechanics and phase-field equations are algorithmically decoupled [51, 83]. In the staggered scheme, we advance the numerical solution from time t_n to t_{n+1} through the following steps:

1. Determine the local history field $\mathcal{H}$ from the displacement variable $\boldsymbol{u}$ at time t_n;
2. Update the current phase-field variable d at time t_{n+1} with Equation (11); and
3. Compute the displacement field $\boldsymbol{u}$ and pore pressure field p at time t_{n+1} by solving Equations (1) and (2) with the updated phase-field variable d.

Even though it requires a more refined mesh [2, 141] and smaller load increments than those required by the monolithic scheme [2, 51], the incremental cost engendered with the staggered scheme is offset by its strong convergence properties and more numerically robust nature especially when the phase-field variable is evolving rapidly [13].

3 Compaction band in a heterogeneous sample

Previous studies have shown that heterogeneous samples are more prone to strain localization than homogeneous samples. Heterogeneity can be in the form of spatially varying density, specific volume, and/or degree of saturation [22, 33, 105, 106]. In this section, we calibrate the model against a dry a rock sample with a spatially varying porosity and show that the predicted variation in porosity resulting from the formation of a compaction band is consistent with that observed in the experiment.

3.1 Calibration using dry Mount Gambier limestone

Several authors have observed a significantly lower porosity within the compaction band as compared to the surrounding host rock [9, 40, 55, 121]. In particular, Chen et al. [30] presented the porosity evolution along the vertical direction in samples of Mount Gambier limestone during triaxial compaction tests. They highlighted that the compaction bands in Mount Gambier limestone form in areas with higher initial porosity. In contrast, sections of the sample with lower initial porosity had negligible changes in porosity after the compression test.

Chen et al. [30] only presented the spatial variation of porosity in the vertical direction (i.e., along the axis of the sample), and not in 3D, and so, in this section we conducted plane strain simulations of compaction band formation in the limestone sample. The rectangular sample is 25.4 mm tall

and 12.7 mm wide, and is divided into a structured mesh with 11,781 four-node quadrilateral finite elements. The smallest element length was 0.5 mm. We followed the suggestion that l_0 be no smaller than no less than twice the characteristic length of the mesh [83, 84] and set it to be $l_0 = 1$ mm. The top and bottom edges of the mesh were supported on vertical rollers and a bottom corner node was pinned for stability. The samples tested by Chen et al. [30] were dry, and so we suppressed the pore pressure degree of freedom in the simulation. A confining pressure of 5 MPa was applied to the sample, which was then deformed at a strain rate of $1.2\text{x}10^{-4}$ s^{-1}.

We calibrated the material parameters of the model using the following procedure. The elastic parameters, the Lamé parameter, and the shear modulus were simply evaluated on the initial linear part of the stress-strain curve shown in Figure 1. The following values were inferred: Lamé parameter $\lambda = 68$

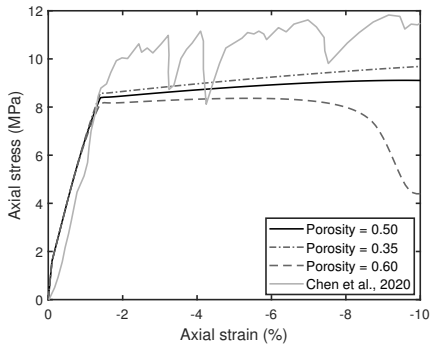

Fig. 1. Single-element stress-strain responses of dry Mount Gambier limestone under a confining pressure of 5 MPa at different porosities. The gray solid line represents the experimental data from Chen et al. [30].

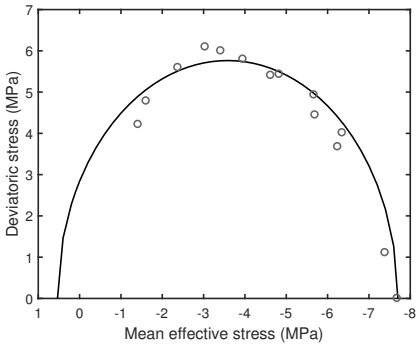

Fig. 2. Calibrated MCC model for simulated samples of Mount Gambier limestone. Ticks are data points from Chen et al. [30].

MPa and shear modulus $\mu = 270$ MPa. Next, the plastic yield surface was calibrated against the experimental yield envelope obtained from triaxial tests [30]. We plot the experimental data and the model yield surface in Figure 2, in which the following MCC parameters were obtained: $M = 1.4$, $p_{c0} = -7.7$ MPa, $p_t = 0.5$ MPa. The plastic compressibility parameter λ^p is one of the parameters controlling the hardening/softening response of the MCC model. We assumed that the initial hardening observed in the stress-strain curve is due mainly to the evolution in the plastic strain and neglect the effect of the evolution of the phase-field variable (which should be small at this point in the loading test). Thus, we simulated single-element tests to calibrate $\lambda^p = 0.28$ against the initial slope of the stress-strain curve immediately after plastic strains are observed. Lastly, the phase-field compressibility parameters λ^d as well as the the breakage parameters θ and average $\mathcal{G}_c$ were determined from the compaction band formation response of the plane strain simulations to be $\theta = 0.9$ and $\mathcal{G}_c = 1.3$ N/mm. We note that developing a more rigorous procedure for calibrating the model is ongoing research and will be investigated in a future study. The single-element stress-strain response using the calibrated material parameters is presented in Figure 1, along with stress-strain curves associated with the end-member porosities $\phi = 0.35$ and $\phi = 0.6$.

In addition, we imposed a spatially varying porosity field that followed the initial spatial distribution measured by Chen et al. [30]. The authors only measured the variation of porosity along the vertical direction; thus, we used a random function generator to obtain a normal distribution of the porosity field in the horizontal direction (i.e., along the width of the plane strain sample), which was then prescribed at the Gauss integration points. The generated spatial field had a mean value of 0.5, a standard deviation of 0.05, and a range of $[0.35, 0.59]$. Several studies investigating breakage and fracture in various materials have suggested a dependence between porosity and the critical energy release rate $\mathcal{G}_c$ [96, 98, 128]. Thus, we assume that

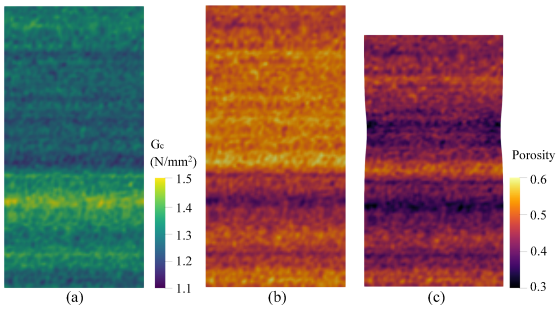

Fig. 3. Contours of material parameters for simulated samples of Mount Gambier limestone under a confining pressure of 5 MPa: (a) the critical energy release rate $\mathcal{G}_c$ in the initial state, (b) porosity ϕ(a) in the initial state, and (c) porosity at a vertical strain of 10%.

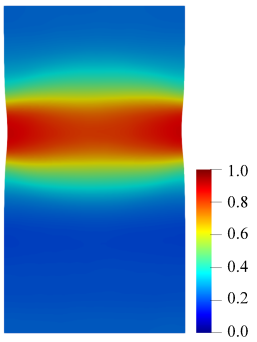

Fig. 4. Contours of phase-field variable d for simulated samples of Mount Gambier limestone under a confining pressure of 5 MPa at a vertical strain of 10%.

the critical energy release rate $\mathcal{G}_c$ also varies spatially following the initial porosity field with a negative relationship, but does not evolve with porosity. The spatial variation of $\mathcal{G}_c$ has a mean value of 1.3 N/mm, a standard deviation of 0.07 N/mm, and a range of $[1.16, 1.51]$ N/mm. Figures 3(a) and (b) present the spatial distributions of $\mathcal{G}_c$ and initial porosity in 2D, respectively.

The plane-strain sample was loaded to a vertical strain of 10% and the phase-field contours are presented in Figure 4. We observe a horizontal zone of grain crushing oriented perpendicular to the direction of maximum compressive stress forming at a distance of around 10 mm below the top of the sample. The zone of grain crushing has a significantly decreased porosity, as seen in Figure 3(b). A comparison of the porosity in the vertical direction before and after the compression test is presented in Figure 5. We note that, similar to the experimental results, a significant decrease in porosity is observed in the compaction band, with an average porosity of 0.36 within the band. Still, there are differences between the simulated sample and the experimental results. The area of reduced porosity in the experiment was thinner than the area of reduced porosity predicted in our simulations. The compaction band formed between 8 to 15 mm below the top of the experimental sample, whereas in our simulations the sample had reduced porosity between 6 to 16 mm below the top of the sample. In addition, areas outside of the compaction band undergo some porosity reduction in our simulation, while there is negligible porosity change outside the compaction band in the experimental data. This behavior in our model is due to the initial hardening of the material within the compaction band when it first forms. The compaction band zone has a higher strength than the rest of the sample and as a result, some of the damage is diffused to the material in the rest of the sample. Furthermore, the ends of the experimental sample showed significant porosity decrease, likely due to end effects that were not captured in the simulations. Nevertheless, this example shows that the proposed model can predict the general trend in

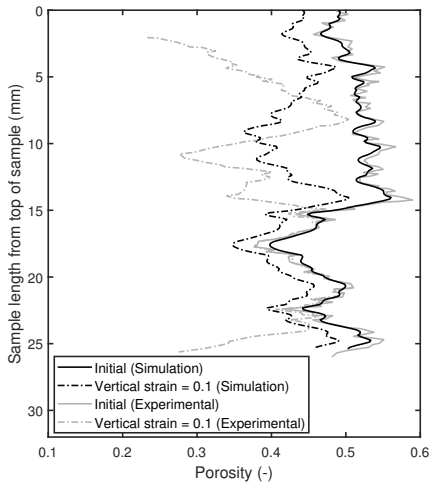

Fig. 5. Variation of porosity along the vertical direction for samples of Mount Gambier limestone under a confining pressure of 5 MPa. Black curves are simulation results; gray curves are experimental measurements [30].

porosity reduction including the likely position of the compaction band in a heterogeneous sample.

3.2 Saturated Mount Gambier limestone

We consider the same compression test on Mount Gambier limestone, but now assume a hypothetical scenario in which the rock was fully saturated. We then investigate its response under globally drained, globally undrained, and locally undrained conditions. We note that the results presented in this section are purely predictions of the rock's response in fully saturated conditions. To the authors' knowledge, no measurements of the pore pressure evolution in porous rocks during compaction band formation are available in the literature. As such, we are unable to validate our model predictions at this time.

In the simulations, the effective confining pressure was maintained at 5 MPa and the pore fluid pressure at the start was zero. The same strain rate and material properties as in the dry sample were assumed for the globally drained and undrained samples, while the hydraulic parameters were assumed to be $f = 7.9\text{x}10^{-5}$, $D_{\max} = 0.15$ mm, and $D_{\min} = 0.015$ mm, which gives an undamaged intrinsic permeability of $8.9\text{x}10^{-13}$ m^2 at a porosity of 0.5 [29]. For the locally undrained sample, we set the sample's intrinsic permeability to zero.

In the globally drained case, fluid was free to flow out of the top and bottom edges of the sample, but not on the vertical sides. Figure 6 presents

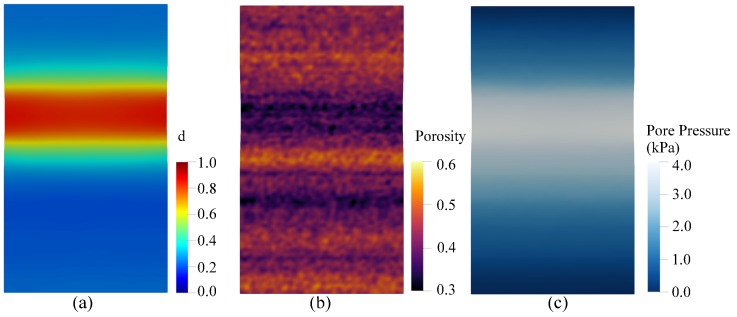

Fig. 6. Globally drained: Contours of the (a) phase-field variable d, (b) porosity ϕ, and (c) pore pressure for simulated samples of fully saturated Mount Gambier limestone under an effective confining pressure of 5 MPa at a vertical strain of 11.8%.

the contours of the phase-field variable, porosity, and pore pressure in the fully saturated sample when it was loaded to a vertical strain of 11.8%. We observe similar results to the simulated case with the dry Mount Gambier limestone sample but at a larger axial strain. A horizontal compaction band forms near the middle of the sample where the area of high initial porosity is located. Due to the high permeability of the sample, the pore fluid is able to drain away quickly as compared to the loading rate. As a result, there is little buildup of pore pressure within the compaction band after it has formed.

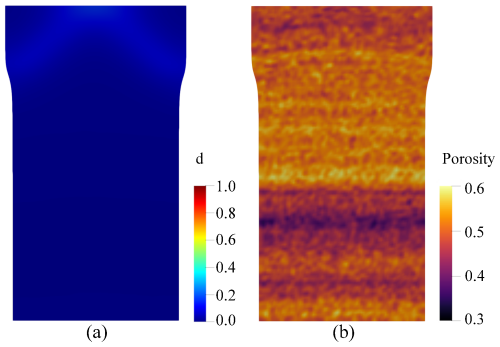

Fig. 7. Globally undrained: Contours of the (a) phase-field variable d and (b) porosity ϕ for simulated samples of fully saturated Mount Gambier limestone under an effective confining pressure of 5 MPa at a vertical strain of 3.3%.

In the globally undrained situation, fluid was prevented from flowing in or out of the sample, but was free to flow within the sample. The contours of

the phase-field variable and porosity at a vertical strain of 3.3% are presented in Figure 7. The pore pressure in the sample is homogeneous at 4.4 MPa. No compaction band is observed in the sample based on the evolution of the phase-field variable. Instead, conjugate oblique bands of significant equivalent plastic strains are seen transecting the upper half of the sample, which is shown in Figure 8(a). As such, the globally undrained sample develops conjugate shear bands instead of a compaction band. Further evidence of shear bands forming in the sample can be seen in the contours of volumetric and deviatoric strains presented in Figures 8(b) and 8(c). The conjugate oblique bands has significant deviatoric strains and low compressive strains, which is characteristic of shear bands [3, 5]. Undrained conditions in the sample lead to a significant buildup of pore pressures in the sample, which reduces the effective stresses in the sample. This affects the local stress paths and can result in the stress points intersecting the modified Cam-Clay yield surface near the critical state line, where little volumetric strains occur. We highlight the model's ability to capture the formation and propagation of shear bands in spite of the free energy decomposition being formulated for compaction bands. While the phase-field variable does not evolve significantly during the propagation of a shear band, the slight increase of the phase-field variable regularizes the zone where the shear band forms. As a result, our phase-field model is able to capture shear band formation without any additional finite element enhancements.

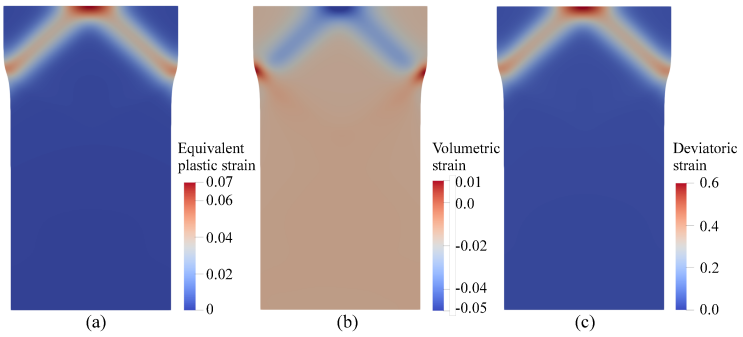

Fig. 8. Globally undrained: Contours of the (a) equivalent plastic strain, (b) volumetric strain and (c) deviatoric strain for simulated samples of fully saturated Mount Gambier limestone under an effective confining pressure of 5 MPa at a vertical strain of 3.3%.

For the locally undrained sample, the intrinsic permeability was set to zero to simulate fluid being trapped in the pores of the rock matrix. Figure 9 presents the contours of the phase-field variable, porosity, and pore pressure in the sample when it was deformed to a vertical strain of 4.0%. Similar to

the globally undrained case, no compaction band is observed for the locally undrained sample. Instead, conjugate shear bands of significant equivalent plastic strains develop at the top of the sample, as shown in Figure 10(a). From Figures 10(b) and 10(c), we observe that these shear bands are also characterized by significant deviatoric strain and little volumetric strain as compared to the surrounding material. We note that there is buildup of pore pressure in the upper portion of the sample, most significantly in the area of breakage where the shear bands initiate.

The above simulation results highlight the effect of drainage conditions on compaction band formation in highly porous rocks. Undrained conditions, both globally and locally, can cause a buildup of pore pressures in the sample, which may inhibit pore collapse and compaction band formation. Instead, a shear band may form in the globally undrained sample due to changes in the stress paths and changes in the locations where the stress paths intersect the yield surface.

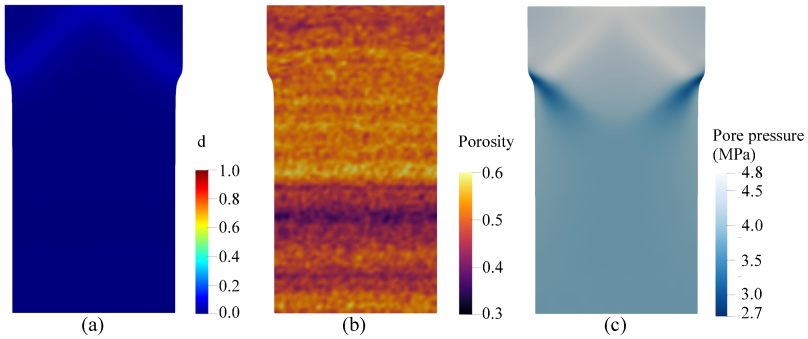

Fig. 9. Locally undrained: Contours of the (a) phase-field variable d, (b) porosity ϕ, and (c) pore pressure for simulated samples of fully saturated Mount Gambier limestone under an effective confining pressure of 5 MPa at a vertical strain of 4.0%.

4 Parametric studies

This section elucidates the effect of compaction band formation on the evolution of pore pressure, porosity, and permeability of a rock. All simulations were conducted in plane strain under vertical compression on fully saturated rock samples. The material parameters chosen are generally similar to those of Bentheim sandstone for illustrative purposes.

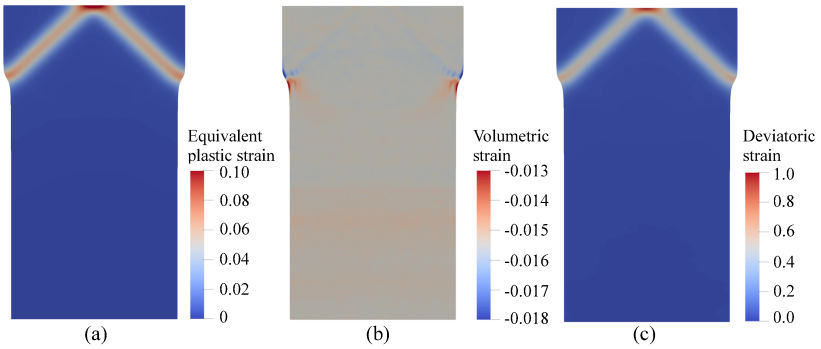

Fig. 10. Locally undrained: Contours of the (a) equivalent plastic strain, (b) volumetric strain and (c) deviatoric strain for simulated samples of fully saturated Mount Gambier limestone under locally undrained conditions and an effective confining pressure of 5 MPa at a vertical strain of 4.0%.

4.1 Drained compression tests on notched samples

We consider a rectangular block 80 mm tall and 40 mm wide with notches on both sides. The notches have a rectangular shape 0.8 mm thick and 2 mm wide. The geometry is divided into 13,713 quadrilateral finite elements. The top and bottom edges of the mesh were supported on vertical rollers, while the bottom corner node was also pinned for stability.

Several numerical simulations of drained samples were conducted varying the effective confining pressure. The following elastoplastic material parameters were assumed in the simulations: Lamé parameter $\lambda = 8000$ MPa, shear modulus $\mu = 7000$ MPa, $\mathcal{G}_c/l_0 = 0.8$ MPa, $l_0 = 1$ mm, $M = 1.2$, $\lambda^p = 0.2$, $\lambda^d = 1.0$, $p_{c0} = -65$ MPa, $p_t = 10$ MPa [36, 86]. The hydraulic parameters were assumed to be: $f = 2\text{x}10^{-4}$, $D_{\max} = 0.2$ mm, and $D_{\min} = 0.01$ mm [80, 115]. Additionally, the following values were used for the porosity $\phi = 0.22$ and Biot coefficient $b = 0.77$ [107]. An initial pore pressure of 5 MPa was applied to the entire sample at the beginning of the simulation. Pore fluid was free to flow out of the top and bottom edges of the sample, but not on the vertical sides. During the simulation, we applied a pore pressure of 5 MPa on the top and bottom edges of the samples and a compressive strain along the vertical axis at a strain rate of $1.25\text{x}10^{-3}$ s^{-1}.

Figure 11 presents the contours of the phase-field variable showing the zones of grain crushing for different values of effective confining pressure, $\sigma' =$ 11, 13, and 16 MPa. Various grain crushing patterns can be seen at different effective confining pressures, with deformation band angles ranging between zero at $\sigma' = 16$ MPa, to 31° at $\sigma' = 11$ MPa. An increase in the effective confining pressure results in the formation of a lower angle compaction band. The results are similar to experimental observations of compaction bands in porous rocks, with low- or high-angled bands forming at lower effective

confining pressure, and horizontal bands forming at higher effective confining pressures [7, 74, 102, 104, 122].

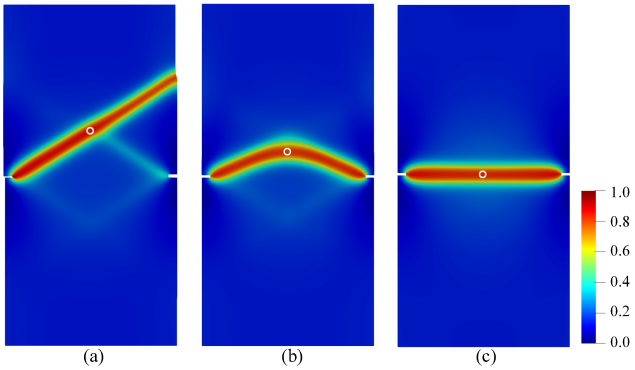

Fig. 11. Contours of phase-field parameter d for samples under a pore pressure of 5 MPa and effective confining pressures of: (a) 11 MPa at a vertical strain of 0.86%; (b) 13 MPa at a vertical strain of 0.50%; and (c) 16 MPa at a vertical strain of 0.47%.

We present the spatiotemporal evolution of the phase-field variable in the sample under an effective confining pressure of 13 MPa in Figure 12. Similar to the results in Ip and Borja [62], we observe that the compaction band initiates at the notches and propagates through the width of the sample. We also note that the band first propagates across the sample with little evolution of the phase-field variable, then the entire band develops into a compaction band with significant breakage and evolution in the phase-field variable. This behavior is likely due to pore pressures building up in the regions with higher breakage and hindering further evolution of the phase-field variable. Consequently, breakage develops evenly across the sample first.

The variations of vertical stress versus vertical strain for the drained samples are presented in Figure 13. We note that the shape of the stress-strain curves are similar for all effective confining pressures. The strains at which the peak vertical stress is achieved differ slightly between samples. The sample with the highest effective confining pressure ($\sigma' = 16$ MPa) experiences peak vertical strain at a lower vertical strain than the other samples. Simultaneously, the pure compaction band in this sample initiates at lower strains.

Figure 14 plots the contours of pore pressures in the drained samples at different effective confining pressures. Higher pore pressures are observed inside and around the compaction band in all the samples. This is due to lower permeabilities in the zones of localized deformation where both the porosity and the average grain diameter (as a result of breakage) are smaller. The pore fluid is essentially trapped in the compaction band during band propagation as there is insufficient time for diffusion of pore fluid out of the zone of localized

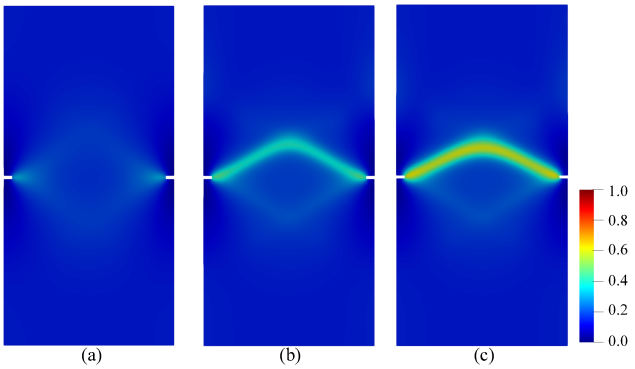

Fig. 12. Contours of phase-field parameter d for samples under pore pressure of 5 MPa and effective confining pressure of 13 MPa at vertical strains of (a) 0.25%; (b) 0.31%; and (c) 0.38%.

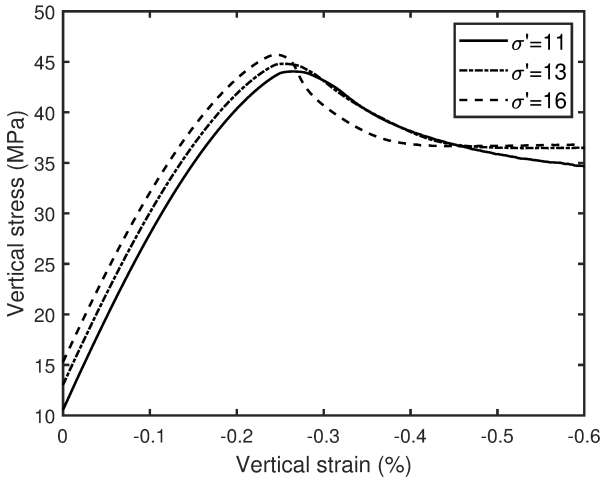

Fig. 13. Variations of vertical stress versus vertical strain for plane-strain compression of drained samples with effective confining pressures of 11, 13, and 16 MPa under pore pressures of 5 MPa.

deformation. The sample with effective confining pressure of 13 MPa exhibits the highest pore pressures when the compaction band has fully propagated with an excess pore water pressure of 0.3 MPa.

To elucidate the evolution of pore pressures inside the band, we plot the local pore pressures in the middle of the compaction band for each sample in Figure 15. The locations in the compaction bands are indicated by the white circles in Figure 11. The pore pressure responses differ greatly between the different samples. The sample with a pure compaction band ($\sigma' = 16$ MPa)

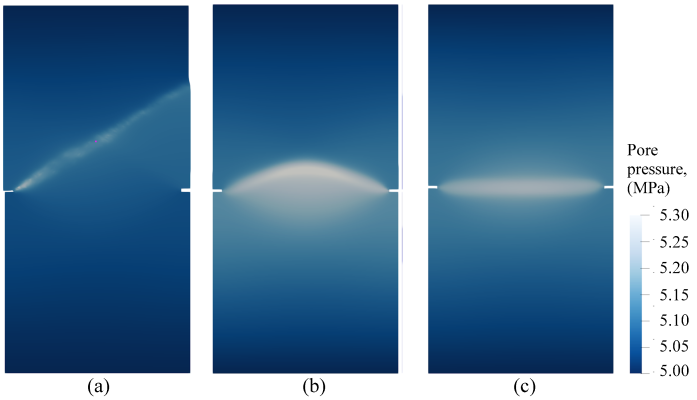

Fig. 14. Contours of pore pressure for samples under a pore pressure of 5 MPa and effective confining pressures of: (a) 11 MPa at a vertical strain of 0.86%; (b) 13 MPa at a vertical strain of 0.50%; and (c) 16 MPa at a vertical strain of 0.47%.

exhibits a sharp spike in the pore pressure upon compaction band initiation, after which the pore pressure also drops sharply and continues to decrease as the compaction band propagates through the sample. Similarly, the sample with the chevron band ($\sigma' = 13$ MPa) shows a large, but less sudden, increase in pore pressure when the band initiates. The dissipation of the excess pore pressure is also more gradual as the band propagates. On the other hand, upon

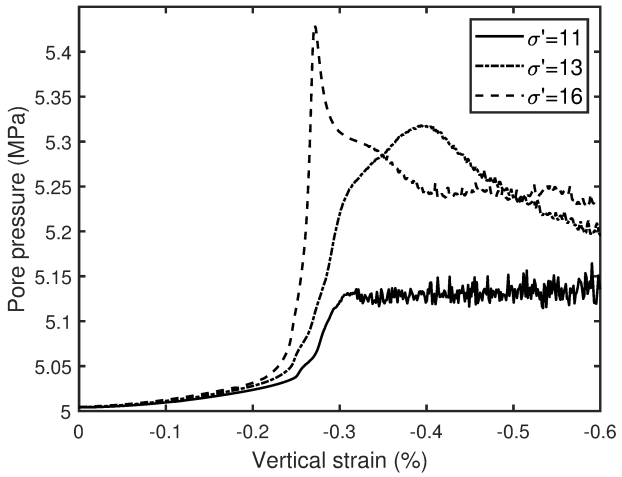

Fig. 15. Variations of pore pressures inside the compaction band during plane strain compression of samples with effective confining pressures of 11, 13, and 16 MPa under a pore pressure of 5 MPa.

band initiation, the sample with the shear-enhanced compaction band ($\sigma' =$ 11 MPa) only experiences a small increase in pore pressure that continues to increase as the band propagates through the sample. The difference in pore pressure evolution in the compaction bands is likely due to the rate at which porosity and permeability decrease in a compaction band when it forms. If there is sudden pore collapse, pore pressures would immediately build up in the compaction band. It would take some time for the pore pressures to dissipate as pore collapse is accompanied by a decrease in permeability. On the other hand, if pore collapse occurs gradually, the pore pressure can dissipate more easily during formation and propagation of the compaction band.

We present the contours of porosity in the sample with a chevron band in Figure 16 to highlight the evolution of porosity during the compression test. There is a significant reduction in porosity within the compaction band to around 10% after the band is fully propagated, which is similar to experimental observations of 10–15% porosity within compaction bands in Bentheim sandstone [107]. We note that the greatest reduction in porosity occurs at the notches of the samples as the compaction band initiates from those regions.

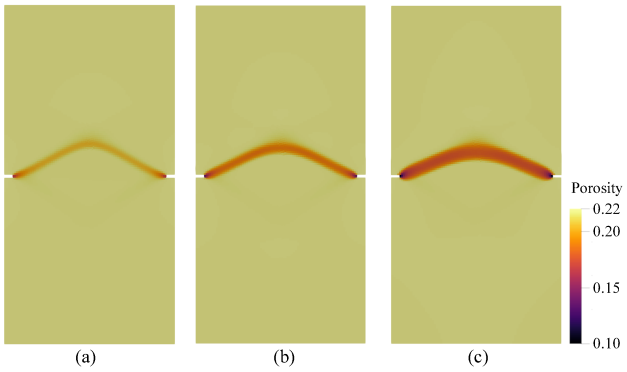

Fig. 16. Contours of porosity for samples under pore pressure of 5 MPa and effective confining pressures of 13 MPa at vertical strains of (a) 0.25%; (b) 0.31%; and (c) 0.38%.Contours of flow velocity vectors during compaction band formation for samples under pore pressure of 5 MPa and effective confining pressures of 13 MPa at vertical strains of (a) 0.25%; (b) 0.31%; (c) 0.38%; and (d) 0.50%.

The evolution of the fluid velocity in the vicinity of the chevron compaction band during its formation and propagation is presented in Figure 17 at the same axial strains as presented in Figures 11(b) and 12. We observe the highest velocities during the initial propagation of the compaction band across the sample around an axial strain of 0.31% in Figure 17(b). As the material in the compaction band region begins to crush, the pore pressure builds up in the compaction band region and there is a larger pressure gradient at the edge of the compaction band. Consequently, the fluid velocity is higher in

that region as fluid flows away from the compaction band. During the initial compaction band propagation, fluid is mostly flowing towards the top of the sample away from the compaction band. As the band continues to propagate and fully develops, the fluid velocity magnitude is highest along the lower edge of the compaction band, where fluid is moving towards the bottom of the sample. The major direction of fluid flow away from the compaction band is likely influenced by the shape of the compaction band that develops.

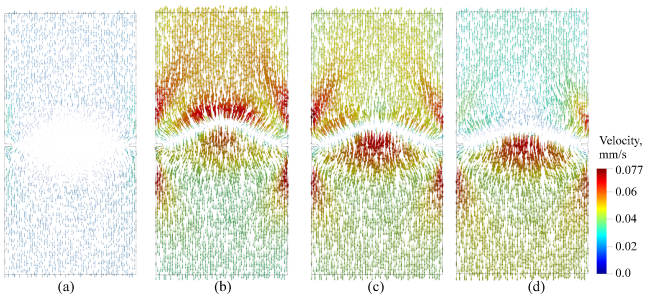

Fig. 17. Contours of flow velocity vectors during compaction band formation for samples under pore pressure of 5 MPa and effective confining pressures of 13 MPa at vertical strains of (a) 0.25%; (b) 0.31%; (c) 0.38%; and (d) 0.50%.

4.2 Permeability reduction

To understand the effects of compaction band formation and propagation on the sample permeability, we evaluated the flow field at different axial strains using a permeability test. Simulations of steady-state fluid flow were performed by applying 1 MPa and zero pore pressure at the top and bottom boundaries of the sample, respectively. The effects of gravity were ignored. Darcy's law was then used to estimate the sample permeability from the average flow velocity out of the sample at nodal points along the bottom boundary.

Figure 18 presents the evolution of permeability in samples at different effective confining pressure. All the samples experience considerable permeability reduction of around two orders of magnitude, similar to experimental measurements of porous sandstones [8, 115, 139]. The relationship between the vertical stress and the permeability is similar to that of experimental measurements of Bentheim sandstone [8, 115], where the sample experiences a substantial reduction in permeability upon compression of the sample, while after the onset of the compaction band, there is a smaller reduction in permeability. The compaction band shape (controlled by the effective confining pressure) has a significant effect on the decrease in permeability, mainly due to the magnitude of strain required for the compaction band to fully propagate through the sample.

The flow velocity vectors in each sample during the permeability test at the end of compaction band propagation are shown in Figure 19 to further investigate fluid flow in and around the compaction band. We note that the magnitudes of flow velocities are generally lower inside the compaction band due to the lower permeability inside the band. Additionally, the contours of flow velocities are similar in the samples with chevron and pure compaction bands. On the other hand, the shear-enhanced compaction band exhibits higher flow velocity along the right edge of the sample.

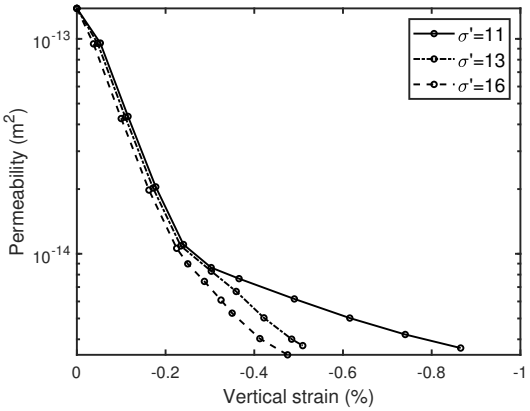

Fig. 18. Variations of intrinsic permeability versus vertical strain for plane-strain compression of samples with effective confining pressures of 11, 13, and 16 MPa under pore pressures of 5 MPa.

4.3 Compaction band can form without softening

This section demonstrates that softening is not a necessary condition for the formation of a compaction band. To this end, numerical simulations of a drained sample was conducted under an effective confining pressure of 16 MPa, assuming the same material parameters as in the previous simulations except for $\lambda^p = 0.01$, $\lambda^d = 1000$ and $\theta = 0.8$. A constant pore pressure of 5 MPa was applied on the top and bottom surfaces of the sample. The sample was also compressed at a strain rate of $1.25\text{x}10^{-3}$ s^{-1}. Figures 20 and 21 present the contours of the phase-field parameter and the stress-strain response of the sample, respectively. We observe double chevron-shaped bands forming between the notches. Significant breakage is also observed in the sample around the compaction band, instead of being concentrated only within the compaction band. The stress-strain response of the sample shows no softening or hardening and resembles a perfectly plastic behavior of the material. This is likely due to having a large λ^d, which reduces the effect of breakage

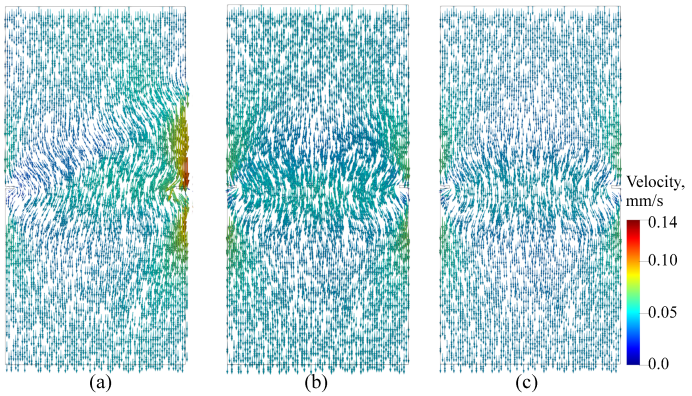

Fig. 19. Contours of flow velocity vectors during permeability tests of samples under pore pressure of 5 MPa and effective confining pressures of: (a) 11 MPa at a vertical strain of 0.86%; (b) 13 MPa at a vertical strain of 0.50%; and (c) 16 MPa at a vertical strain of 0.47%.

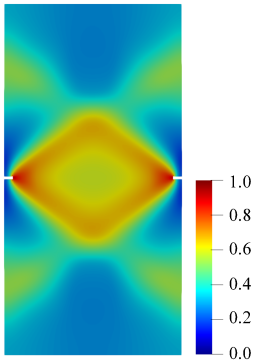

Fig. 20. Contour of phase-field parameter d for a drained sample undergoing plane-strain compression under pore pressure of 5 MPa and effective confining pressure of 16 MPa at a vertical strain of 0.87%.

on degrading the preconsolidation pressure. The small λ^p also amplifies the hardening response of the material upon plastic straining. However, we do not observe hardening in the stress-strain response as the breakage occurs in a more diffuse manner. Since the damaged material does not soften, breakage does not concentrate only in one area and a significant portion of the sample is partially damaged. As a result, the stress-strain response of the sample appears to be perfectly plastic.

To sum up, we have shown that the proposed model can reproduce a compaction band even without softening, in agreement with some laboratory observations reported in the literature [7, 9, 47, 111, 114].

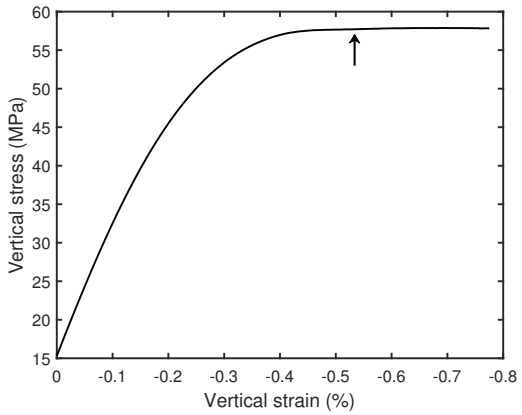

Fig. 21. Variation of vertical stress versus vertical strain for plane-strain compression of a drained sample with an effective confining pressure of 16 MPa under a pore pressure of 5 MPa. Arrow indicates the strain at which the compaction band initiates.

5 Conclusion

In this paper, we have extended the phase-field framework for modeling compaction band formulation developed by Ip and Borja [62] to account for hydromechanical effects, heterogeneity, and permeability reduction in the compaction band. The formulation uses the Kozeny-Carman equation to model the permeability reduction upon grain crushing in the compaction band. Numerical examples on Mount Gambier limestone highlight the model's ability to capture compaction band formation in samples with spatially varying porosity under fully drained, locally undrained and globally undrained conditions. This example is unique in that no artificial material or geometric imperfection was introduced in the sample; instead, the compaction band was reproduced from the sample's inherent heterogeneity similar to the shear band that was reproduced for sand with a spatially varying density [22]. Additionally, the model can capture the transition between shear-enhanced and pure compaction bands with increasing effective confining pressure that has been observed in laboratory experiments. The results presented in this paper also highlight the model's ability to capture the permeability reduction and buildup of pore pressures associated with compaction band formation. Further work is underway to investigate the influence of the material parameters on the band thickness in lab and field scale studies as well as extend the proposed hydromechanical framework to accommodate material anisotropy [50, 103, 133, 137], viscoplasticity [23, 95, 127], chemical reaction [24, 31], and inertia effects [116].

Acknowledgements

This work is supported by the U.S. National Science Foundation under Award Number CMMI-1914780.

Data availability statement

The datasets generated during the course of this study are available from the corresponding author upon reasonable request.

References

[1] Abdallah Y, Sulem J, Bornert M, Ghabezloo S, Stefanou I (2021). Compaction banding in high-porosity carbonate rocks: 1. Experimental observations. Journal of Geophysical Research: Solid Earth 126: e2020JB020538

[2] Ambati M, Gerasimov T, De Lorenzis L (2015). A review on phase-field models of brittle fracture and a new fast hybrid formulation. Computational Mechanics 55(2):383–405.

[3] Antonellini MA, Aydin A, Pollard DD (1994). Microstructure of deformation bands in porous sandstones at Arches National Park, Utah. Journal of structural geology 16(7):941-59.

[4] Arriaga M, Waisman H (2018). Multidimensional stability analysis of the phase-field method for fracture with a general degradation function and energy split. Computational Mechanics 61(1–2):181–205.

[5] Aydin A, Borja RI, Eichhubl P (2006). Geological and mathematical framework for failure modes in granular rock. Journal of Structural Geology 28(1):83–98.

[6] Baud P, Zhu W, Wong TF (2000). Failure mode and weakening effect of water on sandstone. Journal of Geophysical Research: Solid Earth, 105(B7):16371-16389.

[7] Baud P, Klein E, Wong TF (2004). Compaction localization in porous sandstones: spatial evolution of damage and acoustic emission activity. Journal of Structural Geology 26(4):603–624.

[8] Baud P, Meredith P, Townend E (2012). Permeability evolution during triaxial compaction of an anisotropic porous sandstone. Journal of Geophysical Research: Solid Earth 117(B5).

[9] Baxevanis T, Papamichos E, Flornes O, Larsen I (2006). Compaction bands and induced permeability reduction in Tuffeau de Maastricht calcarenite. Acta Geotechnica 1(2):123–135.

[10] Bear J (1972). Dynamics of Fluids in Porous Media, American Elsevier Publishing Company, Inc., New York, NY.

[11] Bésuelle P, Desrues J, Raynaud S (2000). Experimental characterisation of the localisation phenomenon inside a Vosges sandstone in a triaxial cell. International Journal of Rock Mechanics and Mining Sciences 37(8): 1223-1237.

[12] Bilgen C, Weinberg K (2019). On the crack-driving force of phase-field models in linearized and finite elasticity. Computer Methods in Applied Mechanics and Engineering 353:348-372.

[13] Borden MJ, Hughes TJ, Landis CM, Anvari A, Lee IJ (2016). A phase-field formulation for fracture in ductile materials: Finite deformation balance law derivation, plastic degradation, and stress triaxiality effects. Computer Methods in Applied Mechanics and Engineering 312:130–166.

[14] Borja RI, Lee SR (1990). Cam-Clay plasticity, Part 1: Implicit integration of elasto-plastic constitutive relations. Computer Methods in Applied Mechanics and Engineering 78(1):49–72.

[15] Borja RI (1991). Cam-Clay plasticity, Part II: Implicit integration of constitutive equation based on a nonlinear elastic stress predictor. Computer Methods in Applied Mechanics and Engineering 88(2):225–240.

[16] Borja RI (2000). A finite element model for strain localization analysis of strongly discontinuous fields based on standard Galerkin approximation. Computer Methods in Applied Mechanics and Engineering 190(11–12):1529–1549.

[17] Borja RI, Regueiro RA (2001). Strain localization in frictional materials exhibiting displacement jumps. Computer Methods in Applied Mechanics and Engineering 190(20–21):2555–2580.

[18] Borja RI, Aydin A (2004). Computational modeling of deformation bands in granular media, I: Geological and mathematical framework. Computer Methods in Applied Mechanics and Engineering 193(27–29):2667–2698.

[19] Borja RI (2004). Computational modeling of deformation bands in granular media, II: Numerical simulations. Computer Methods in Applied Mechanics and Engineering 193(27–29):2699–2718.

[20] Borja RI (2008). Assumed enhanced strain and the extended finite element methods: A unification of concepts. Computer Methods in Applied Mechanics and Engineering 197(33–34):2789–2803.

[21] Borja RI (2013). Plasticity Modeling & Computation. Springer, Berlin-Heidelberg.

[22] Borja RI, Song X, Rechenmacher AL, Abedi S, Wu W (2013). Shear band in sand with spatially varying density. Journal of the Mechanics and Physics of Solids 61(1):219–234.

[23] Borja RI, Yin Q, Zhao Y (2020). Cam-Clay plasticity. Part IX: On the anisotropy, heterogeneity, and viscoplasticity of shale. Computer Methods in Applied Mechanics and Engineering 360:112695.

[24] Borja RI, Chen W, Odufisan AR (2023). A constitutive framework for rocks undergoing solid dissolution. Journal of the Mechanics and Physics of Solids 173:105198.

[25] Bourdin B, Francfort GA, Marigo JJ (2000). Numerical experiments in revisited brittle fracture. Journal of the Mechanics and Physics of Solids 48(4):797-826.

[26] Carman P (1937). Fluid flow through granular beds. Trans, Inst. Chem. Eng., London 15:150-166.

[27] Challa V, Issen KA (2004). Conditions for compaction band formation in porous rock using a two-yield surface model. Journal of engineering mechanics 130(9):1089-1097.

[28] Charalampidou EM, Hall SA, Stanchits S, Lewis H, Viggiani G (2011). Characterization of shear and compaction bands in a porous sandstone deformed under triaxial compression. Tectonophysics 503(1-2):8-17.

[29] Chen X, Roshan H, Regenauer-Lieb K (2019). Permeability evolution of limestone during formation of compaction bands: a digital poro-mechanics approach. In 53rd US Rock Mechanics/Geomechanics Symposium. OnePetro.

[30] Chen X, Roshan H, Lv A, Hu M, Regenauer-Lieb K (2020). The dynamic evolution of compaction bands in highly porous carbonates: the role of local heterogeneity for nucleation and propagation. Progress in Earth and Planetary Science 7(1):1-9.

[31] Chen W, Zhao Y, Borja RI (2023). Solid–fluid interaction in porous materials with internal erosion. Acta Geotechnica, https://doi.org/10.1007/s11440-023-01906-4.

[32] Cheung CS, Baud P, Wong TF (2012). Effect of grain size distribution on the development of compaction localization in porous sandstone. Geophysical Research Letters 39:L21302.

[33] Choo J, White JA, Borja RI (2016). Hydromechanical modeling of unsaturated flow in double porosity media. International Journal of Geomechanics 16(6), https://doi.org/10.1061/(ASCE)GM.1943-5622.0000558.

[34] Choo J, Sun W (2018). Coupled phase-field and plasticity modeling of geological materials: From brittle fracture to ductile flow. Computer Methods in Applied Mechanics and Engineering 330:1-32.

[35] Cilona A, Faulkner DR, Tondi E, Agosta F, Mancini L, Rustichelli A, Baud P, Vinciguerra S (2014). The effects of rock heterogeneity on compaction localization in porous carbonates. Journal of Structural Geology 67:75-93.

[36] Das A, Nguyen GD, Einav I (2011). Compaction bands due to grain crushing in porous rocks: a theoretical approach based on breakage mechanics. Journal of Geophysical Research: Solid Earth 116:B08203.

[37] David C, Wong TF, Zhu W, Zhang J (1994). Laboratory measurement of compaction-induced permeability change in porous rocks: Implications for the generation and maintenance of pore pressure excess in the crust. pure and applied geophysics 143(1):425-56.

[38] Deng S, Zuo L, Aydin A, Dvorkin J, Mukerji T (2015). Permeability characterization of natural compaction bands using core flooding

experiments and three-dimensional image-based analysis: Comparing and contrasting the results from two different methods. Aapg Bulletin 99(1):27-49.

[39] Dresen G, Stanchits S, Rybacki E (2010). Borehole breakout evolution through acoustic emission location analysis. International Journal of Rock Mechanics and Mining Sciences 47(3):426-435.

[40] Eichhubl P, Hooker JN, Laubach SE (2010). Pure and shear-enhanced compaction bands in Aztec Sandstone. Journal of Structural Geology 32(12):1873-1886.

[41] Einav I (2007). Breakage mechanics—part I: theory. Journal of the Mechanics and Physics of Solids 55(6):1274-1297.

[42] Einav I (2007). Breakage mechanics—Part II: Modelling granular materials. Journal of the Mechanics and Physics of Solids 55(6):1298-1320.

[43] Esna Ashari S, Das A, Buscarnera G (2018). Model-based assessment of the effect of surface area growth on the permeability of granular rocks. Journal of Engineering Mechanics 144(5):04018023.

[44] Farquharson JI, Baud P, Heap MJ (2017). Inelastic compaction and permeability evolution in volcanic rock. Solid Earth 8(2):561-81.

[45] Fei F, Choo J (2020). A phase-field model of frictional shear fracture in geologic materials. Computer Methods in Applied Mechanics and Engineering 369:113265.

[46] Fortin J, Stanchits S, Dresen G, Guéguen Y (2006). Acoustic emission and velocities associated with the formation of compaction bands in sandstone. Journal of Geophysical Research: Solid Earth 1111:B10203.

[47] Fortin J, Schubnel A, Guéguen Y (2005). Elastic wave velocities and permeability evolution during compaction of Bleurswiller sandstone. International Journal of Rock Mechanics and Mining Sciences 42(7-8):873-89.

[48] Fossen H, Schultz RA, Torabi A (2011). Conditions and implications for compaction band formation in the Navajo Sandstone, Utah. Journal of Structural Geology 33(10):1477-1490.

[49] Francfort GA, Marigo JJ (1998). Revisiting brittle fracture as an energy minimization problem. Journal of the Mechanics and Physics of Solids 46(8):1319-1342.

[50] Gao Z, Li X, Lu D (2022). Nonlocal regularization of an anisotropic critical state model for sand. Acta Geotechnica 17(2):427-39.

[51] Gerasimov T, De Lorenzis L (2016). A line search assisted monolithic approach for phase-field computing of brittle fracture. Computer Methods in Applied Mechanics and Engineering 312:276-303.

[52] Gerolymatou E, Leuthold J (2021). Compaction localization and anisotropic permeability evolution. Computers and Geotechnics 137:104173.

[53] Haimson B (2001). Fracture-like borehole breakouts in high-porosity sandstone: are they caused by compaction bands?. Physics and Chemistry of the Earth, Part A: Solid Earth and Geodesy 26(1-2):15-20.

[54] Haimson B (2007). Micromechanisms of borehole instability leading to breakouts in rocks. International Journal of Rock Mechanics and Mining Sciences 44(2):157-173.
[55] Heap MJ, Brantut N, Baud P, Meredith PG (2015). Time-dependent compaction band formation in sandstone. Journal of Geophysical Research: Solid Earth 120(7):4808-30.
[56] Hill R (1989). Analysis of deformation bands in the Aztec Sandstone, Valley of Fire State Park, Nevada, MS thesis, Univ. of Nevada, Las Vegas
[57] Holcomb DJ, Costin LS (1986). Detecting Damage Surfaces in Brittle Materials Using Acoustic Emissions. ASME. J. Appl. Mech. 53(3): 536–544.
[58] Holcomb DJ, Olsson WA (2003). Compaction localization and fluid flow. Journal of Geophysical Research: Solid Earth 108(B6).
[59] Holcomb D, Rudnicki JW, Issen KA, Sternlof K (2007). Compaction localization in the Earth and the laboratory: state of the research and research directions. Acta Geotechnica 2(1):1-5.
[60] Horpibulsuk S, Liu MD, Liyanapathirana DS, Suebsuk J (2010). Behaviour of cemented clay simulated via the theoretical framework of the Structured Cam Clay model. Computers and Geotechnics 37(1-2):1-9.
[61] Ip SCY, Choo J, Borja RI (2022). Impacts of saturation-dependent anisotropy on the shrinkage behavior of clay rocks. Acta Geotechnica 16(11):3381–3400.
[62] Ip SCY, Borja RI (2022). A phase-field approach for compaction band formation due to grain crushing. International Journal for Numerical and Analytical Methods in Geomechanics 46(16):2965-87.
[63] Ip SCY, Borja RI (2022). Evolution of anisotropy with saturation and its implications for the elastoplastic responses of clay rocks. International Journal for Numerical and Analytical Methods in Geomechanics 46(1):23–46.
[64] Ip SCY, Borja RI (2023). Multiscale interactions of elastic anisotropy in unsaturated clayey rocks using a homogenization model. Acta Geotechnica, https://doi.org/10.1007/s11440-022-01784-2
[65] Issen KA, Rudnicki JW (2000). Conditions for compaction bands in porous rock. Journal of Geophysical Research: Solid Earth 105(B9):21529–21536.
[66] Juang CH, Holtz RD (1986). A probabilistic permeability model and the pore size density function. International Journal for numerical and analytical methods in geomechanics 10(5):543-53.
[67] Kaminskaite I, Fisher QJ, Michie EA (2019). Microstructure and petrophysical properties of deformation bands in high porosity carbonates. Journal of Structural Geology 119:61-80.
[68] Katsman R, Aharonov E, Scher H (2005). Numerical simulation of compaction bands in high-porosity sedimentary rock. Mechanics of materials 37(1): 143–162.

[69] Katsman R, Aharonov E (2006). A study of compaction bands originating from cracks, notches, and compacted defects. Journal of Structural Geology 28(3):508–518.

[70] Keehm Y, Sternjof K, Mukerji T (2006). Computational estimation of compaction band permeability in sandstone. Geosciences Journal 10(4):499-505.

[71] Khaddour F, Grégoire D, Pijaudier-Cabot G (2018). A hierarchical model for the computation of permeation properties of porous materials and their enhancement due to microcracks. Journal of Engineering Mechanics 144(2):04017160.

[72] Klein E, Baud P, Reuschlé T, Wong TF (2001). Mechanical behaviour and failure mode of Bentheim sandstone under triaxial compression. Physics and Chemistry of the Earth, Part A: Solid Earth and Geodesy 26(1–2): 21–25.

[73] Kozeny J (1927). über kapillare leitung des wasser im boden. Sitzungsberichte Wiener Akademie 136:271–306.

[74] Leuthold J, Gerolymatou E, Vergara MR, Triantafyllidis T (2021). Effect of compaction banding on the hydraulic properties of porous rock: part I—experimental investigation. Rock Mechanics and Rock Engineering 54(6):2671-83.

[75] Leuthold J, Gerolymatou E, Triantafyllidis T (2021). Effect of Compaction Banding on the Hydraulic Properties of Porous Rock-Part II: Constitutive Description and Numerical Simulations. Rock Mechanics and Rock Engineering 54(6):2685-96.

[76] Liu Y, Borja RI (2022). Time scales in the primary and secondary compression of soils. International Journal for Numerical and Analytical Methods in Geomechanics, DOI: 10.1002/nag.3350.

[77] Liu F, Borja RI (2008). A contact algorithm for frictional crack propagation with the extended finite element method. International Journal for Numerical Methods in Engineering 76(10):1489–1512.

[78] Liu F, Borja RI (2010). Stabilized low-order finite elements for frictional contact with the extended finite element method. Computer Methods in Applied Mechanics and Engineering 199(37–40):2456–2471.

[79] Liu C, Pollard DD, Deng S, Aydin A (2015). Mechanism of formation of wiggly compaction bands in porous sandstone: 1. Observations and conceptual model. Journal of Geophysical Research: Solid Earth 120(12): 8138–8152.

[80] Louis L, David C, Robion P (2003). Comparison of the anisotropic behaviour of undeformed sandstones under dry and saturated conditions, Tectonophysics, 370:193 – 212.

[81] Marketos G, Bolton MD (2009). Compaction bands simulated in discrete element models. Journal of structural Geology 31(5):479–490.

[82] Meng F, Baud P, Ge H, Wong TF (2019). The effect of stress on limestone permeability and effective stress behavior of damaged samples. Journal of Geophysical Research: Solid Earth 124(1):376-99.

[83] Miehe C, Welschinger F, Hofacker M (2010). Thermodynamically consistent phase-field models of fracture: Variational principles and multi-field FE implementations. International journal for numerical methods in engineering 83(10):1273–1311.

[84] Miehe C, Hofacker M, Welschinger F (2010). A phase field model for rate-independent crack propagation: Robust algorithmic implementation based on operator splits. Computer Methods in Applied Mechanics and Engineering 199(45-48):2765-78.

[85] Miehe C, Schänzel LM (2014). Phase field modeling of fracture in rubbery polymers. Part I: Finite elasticity coupled with brittle failure. Journal of the Mechanics and Physics of Solids 65:93–113.

[86] Mir A, Nguyen GD, Sheikh AH (2018). A thermodynamics-based model for brittle to ductile behaviour and localised failure of porous rocks. International Journal of Solids and Structures 152:161–184.

[87] Mollema PN, Antonellini MA (1996). Compaction bands: a structural analog for anti-mode I cracks in aeolian sandstone. Tectonophysics 267(1–4): 209–228.

[88] Nanda K, Vaishakh TK, Das A, Misra S (2020). Hydro-mechanical response in porous rocks during localized deformation: finite element analysis. Journal of structural geology 130:103909.

[89] Nguyen GD, Einav I (2009). The energetics of cataclasis based on breakage mechanics. Pure and applied geophysics 166(10):1693–1724.

[90] Nguyen GD, Nguyen CT, Bui HH, Nguyen VP (2016). Constitutive modelling of compaction localisation in porous sandstones. International Journal of Rock Mechanics and Mining Sciences 83:57–72.

[91] Olsson WA (1999). Theoretical and experimental investigation of compaction bands in porous rock. Journal of Geophysical Research: Solid Earth 104(B4):7219–7228.

[92] Olsson WA, Holcomb DJ (2000). Compaction localization in porous rock. Geophysical Research Letters 27(21):3537–3540.

[93] Olsson WA, Holcomb DJ, Rudnicki JW (2002). Compaction localization in porous sandstone: Implications for reservoir mechanics. Oil & Gas Science and Technology 57(5):591–599.

[94] Permann CJ, Gaston DR, Andrš D, Carlsen RW, Kong F, Lindsay AD, Miller JM, Peterson JW, Slaughter AE, Stogner RH, Martineau RC (2020). MOOSE: Enabling massively parallel multiphysics simulation. SoftwareX, 11, 100430.

[95] Prassa C, Alevizos S, Veveakis M, Dafalias YF (2022). The influence of anisotropy on compaction bands: The case of coaxiality between stress and fabric anisotropy tensors. International Journal for Numerical and Analytical Methods in Geomechanics 46(1):68-88.

[96] Rice RW (1996). Grain size and porosity dependence of ceramic fracture energy and toughness at 22 C. Journal of materials science 31:1969-83.

997 [97] Roscoe KH, Burland JB, Heyman J, Leckie FA (1968) On the gener-
998 alized stress-strain behaviour of wet clay. Engineering Plasticity, Cam-
999 bridge: 535–609.
1000 [98] Rice RW (1996). Grain size and porosity dependence of ceramic fracture
1001 energy and toughness at 22 C. Journal of materials science 31:1969-83.
1002 [99] Rudnicki JW, Rice JR (1975). Conditions for the localization of defor-
1003 mation in pressure-sensitive dilatant materials. Journal of the Mechanics
1004 and Physics of Solids 23(6):371–394.
1005 [100] Rudnicki JW, Sternlof KR (2005). Energy release model of compaction
1006 band propagation. Geophysical Research Letters 32:L16303.
1007 [101] Rutqvist J (2012). The geomechanics of CO2 storage in deep sedimen-
1008 tary formations. Geotechnical and Geological Engineering 30(3):525-
1009 551.
1010 [102] Sari M, Sarout J, Poulet T, Dautriat J, Veveakis M (2022). The Brit-
1011 tle–Ductile Transition and the Formation of Compaction Bands in the
1012 Savonnières Limestone: Impact of the Stress and Pore Fluid. Rock Me-
1013 chanics and Rock Engineering 55(11):6541-53.
1014 [103] Shahin, G, Papazoglou, A, Marinelli, F, Viggiani, G, Buscarnera, G
1015 (2022). Experimental study of compaction localization in carbonate rock
1016 and constitutive modeling of mechanical anisotropy. Int J Numer Anal
1017 Methods 46: 2561– 2581. https://doi.org/10.1002/nag.3418
1018 [104] Skurtveit E, Torabi A, Gabrielsen RH, Zoback MD (2013). Experimental
1019 investigation of deformation mechanisms during shear-enhanced com-
1020 paction in poorly lithified sandstone and sand. Journal of Geophysical
1021 Research: Solid Earth 118(8):4083-100.
1022 [105] Song X, Borja RI (2014). Mathematical framework for unsaturated flow
1023 in the finite deformation range. International Journal for Numerical
1024 Methods in Engineering 97(9):658–682.
1025 [106] Song X, Borja RI (2014). Finite deformation and fluid flow in unsat-
1026 urated soils with random heterogeneity. Vadose Zone Journal 13(5),
1027 https://doi.org/10.2136/vzj2013.07.0131.
1028 [107] Stanchits S, Fortin J, Gueguen Y, Dresen G (2009). Initiation and prop-
1029 agation of compaction bands in dry and wet Bentheim sandstone. Pure
1030 and Applied Geophysics 166(5):843-868.
1031 [108] Sternlof KR, Rudnicki JW, Pollard DD (2005). Anticrack inclusion
1032 model for compaction bands in sandstone. Journal of Geophysical Re-
1033 search: Solid Earth 110:B11403.
1034 [109] Sulem J, Ouffroukh H (2006). Shear banding in drained and undrained
1035 triaxial tests on a saturated sandstone: Porosity and permeability evo-
1036 lution. International Journal of Rock Mechanics and Mining Sciences
1037 43(2):292-310.
1038 [110] Taylor G, Quinney H (1937). The latent heat remaining in a metal after
1039 cold work, Proc. R. Soc. Lond. Ser. A 143(834):307–326.
1040 [111] Tembe S, Vajdova V, Wong TF, Zhu W (2006). Initiation and prop-
1041 agation of strain localization in circumferentially notched samples of

two porous sandstones. Journal of Geophysical Research: Solid Earth 111:B02409.

[112] Tembe S, Baud P, Wong TF (2008). Stress conditions for the propagation of discrete compaction bands in porous sandstone. Journal of Geophysical Research: Solid Earth 113(B9).

[113] Tengattini A, Das A, Nguyen GD, Viggiani G, Hall SA, Einav I (2014). A thermomechanical constitutive model for cemented granular materials with quantifiable internal variables. Part I—Theory. Journal of the Mechanics and Physics of Solids 70:281-296.

[114] Vajdova V, Wong TF (2003). Incremental propagation of discrete compaction bands: acoustic emission and microstructural observations on circumferentially notched samples of Bentheim. Geophysical Research Letters 30:1775.

[115] Vajdova V, Baud P, Wong TF (2004). Permeability evolution during localized deformation in Bentheim sandstone. Journal of Geophysical Research: Solid Earth 109(B10).

[116] Wang Y, Borja RI, Wu W (2023). Dynamic strain localization into a compaction band via a phase-field approach. Journal of the Mechanics and Physics of Solids 173:105228.

[117] Wang B, Chen Y, Wong TF (2008). A discrete element model for the development of compaction localization in granular rock. Journal of Geophysical Research: Solid Earth 113:B03202.

[118] White JA, Borja RI (2008). Stabilized low-order finite elements for coupled solid-deformation/fluid-diffusion and their application to fault zone transients. Comput Methods Appl Mech Eng 197:4353–4366

[119] Wilkins A, Green CP, Ennis-King J (2020). PorousFlow: a multiphysics simulation code for coupled problems in porous media. Journal of Open Source Software 5(55):2176.

[120] Wilkins A, Green CP, Ennis-King J (2021). An open-source multiphysics simulation code for coupled problems in porous media. Computers & Geosciences 154:104820.

[121] Wong TF, David C, Zhu W (1997). The transition from brittle faulting to cataclastic flow in porous sandstones: Mechanical deformation. Journal of Geophysical Research: Solid Earth 102(B2):3009-3025.

[122] Wong TF, Baud P, Klein E (2001). Localized failure modes in a compactant porous rock. Geophysical Research Letters 28(13):2521-2524.

[123] Wu H, Guo N, Zhao J (2018). Multiscale modeling and analysis of compaction bands in high-porosity sandstones. Acta Geotech. 13:575–599

[124] Wu H, Zhao J, Guo N (2019). Multiscale modeling of compaction bands in saturated high-porosity sandstones. Engineering Geology 261:105282.

[125] Wu H, Papazoglou A, Viggiani G, Dano C, Zhao J (2020). Compaction bands in Tuffeau de Maastricht: insights from X-ray tomography and multiscale modeling. Acta Geotechnica 15(1):39-55.

[126] Xu Y, Zhou S, Xia C, Hu Y (2022). A new phase field model for mixed-mode brittle fractures in rocks modified from triple shear energy criterion. Acta Geotechnica 17(12):5613-37.

[127] Xue D, Shahin G, Lü X, Buscarnera G (2022). Strain localization criteria for viscoplastic geomaterials. International Journal for Numerical and Analytical Methods in Geomechanics 46(4):717-38.

[128] Yang JF, Ohji T, Kanzaki S, Díaz A, Hampshire S (2002). Microstructure and mechanical properties of silicon nitride ceramics with controlled porosity. Journal of the American Ceramic Society 85(6):1512-6.

[129] Yang H, Sinha SK, Feng Y, McCallen DB, Jeremić B (2018). Energy dissipation analysis of elastic–plastic materials. Computer Methods in Applied Mechanics and Engineering 331:309-326.

[130] Yin Q, Liu Y, Borja RI (2021). Mechanisms of creep in shale from nanoscale to specimen scale. Computers and Geotechnics 136:104138.

[131] You T, Waisman H, Zhu QZ (2021). Brittle-ductile failure transition in geomaterials modeled by a modified phase-field method with a varying damage-driving energy coefficient. International Journal of Plasticity, 136:102836.

[132] Zhai H, Masoumi H, Zoorabadi M, Canbulat I (2020). Size-dependent behaviour of weak intact rocks. Rock Mechanics and Rock Engineering 53:3563-87.

[133] Zhao Y, Semnani SJ, Yin Q, Borja RI (2018). On the strength of transversely isotropic rocks. International Journal for Numerical and Analytical Methods in Geomechanics 42(16):1917-34.

[134] Zhao Y, Borja RI (2020). A continuum framework for coupled solid deformation–fluid flow through anisotropic elastoplastic porous media. Computer Methods in Applied Mechanics and Engineering 369:113225.

[135] Zhao Y, Borja RI (2021). Anisotropic elastoplastic response of double-porosity media. Computer Methods in Applied Mechanics and Engineering 380:113797.

[136] Zhang Q, Borja RI (2021). Poroelastic coefficients for anisotropic single and double porosity media. Acta Geotechnica 16(10):3013–3025.

[137] Zhao Y, Borja RI (2022). A double-yield-surface plasticity theory for transversely isotropic rocks. Acta Geotechnica 17(11):5201-21.

[138] Zhou S, Zhuang X, Rabczuk T (2019). Phase field modeling of brittle compressive-shear fractures in rock-like materials: A new driving force and a hybrid formulation. Computer Methods in Applied Mechanics and Engineering 355:729-52.

[139] Zhu W, Wong TF (1997). The transition from brittle faulting to cataclastic flow: Permeability evolution. Journal of Geophysical Research: Solid Earth, 102(B2):3027-3041.

[140] Zhu W, Wong TF (1999). Network modeling of the evolution of permeability and dilatancy in compact rock. Journal of Geophysical Research: Solid Earth 104(B2):2963-71.

[141] Zhuang X, Zhou S, Huynh GD, Areias P, Rabczuk T (2022). Phase field modeling and computer implementation: A review. Engineering Fracture Mechanics 262:108234.